ACS Photonics

pubs.acs.org/journal/apchd5

Article

Linear Electro-optic Effect in Silicon Nitride Waveguides Enabled by Electric-Field Poling

Boris Zabelich, Edgars Nitiss, Anton Stroganov, and Camille-Sophie Brès*

Cite This: ACS Photonics 2022, 9, 3374−3383

Read Online

ACCESS | Metrics & More | Article Recommendations | Supporting Information

ABSTRACT: Stoichiometric silicon nitride (Si_3N_4) is one of the most mature integrated photonic platforms for linear and nonlinear optical applications on-chip. However, because it is a centrosymmetric material, second-order nonlinear processes are inherently not available in Si_3N_4, limiting its use for multiple classical and quantum applications. In this work, we implement thermally assisted electric-field poling, which allows charge carrier separation in the waveguide core, leading to a depletion zone formation and the inscription of a strong electric field reaching 20 V/μm. The latter results in an effective second-order susceptibility ($\chi^{(2)}$) inside the Si_3N_4 waveguide, making linear electro-optic modulation accessible on the platform for the first time. We develop a numerical model for simulating the poling process inside the waveguide and use it to calculate the diffusion coefficient and the concentration of the charge carriers responsible for the field formation. The charge carrier concentration, as well as the waveguide core size, is found to play a significant role in determining the achievable effective nonlinearity experienced by the optical mode inside the waveguide. Current findings establish a strong groundwork for further advancement of $\chi^{(2)}$-based devices on Si_3N_4.

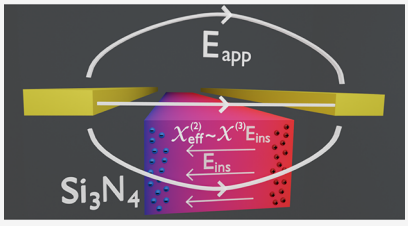

KEYWORDS: *stoichiometric silicon nitride, nonlinear optics, electric-field poling, phase modulation, DC Kerr effect*

INTRODUCTION

Second-order nonlinear optical functionalities realized on a chip are key for enabling a wide variety of photonic-based applications. In particular, the linear electro-optic (EO) effect allows for high-speed modulation and low-power optical phase tuning, which are essential for communications,[1] programmable photonics,[2] and LIDAR,[3] to name a few. Currently, a wide variety of materials and device designs have been considered for making the on-chip EO functionality available.[4] Silicon photonics stands out as having the highest level of technological maturity through complementary metal−oxide−semiconductor (CMOS) technology and process toolsets. CMOS-compatible materials such as silicon (Si), stoichiometric silicon nitride (Si_3N_4), and silicon dioxide (SiO_2) are the primary platforms for the development of photonic integrated circuits strongly motivated by the possibility of CMOS photonics and electronics co-integration.[5−7] While in the vast majority of studies, the mentioned materials have been mainly employed for their third-order nonlinearity,[8] unlocking full functionality of a Si-based photonic chip requires making second-order nonlinear processes accessible, including EO phase modulation and optical three-wave mixing frequency conversion.[5] Although phase modulation in Si can be achieved through the free-carrier plasma dispersion effect,[9] the approach has several drawbacks and limitations, such as the presence of spurious intensity modulation, refractive index modulation chirp, and inherently limited operation bandwidth.[4] Having second-order nonlinearity on a CMOS fabrication process-compatible platform would circumvent these issues, providing routes for achieving broadband and energy-efficient modulation. Additionally, second-order nonlinearity in a Si-based platform would enable many classical and quantum optical applications.[10] While the listed Si-based integrated photonic platforms lack second-order susceptibility ($\chi^{(2)}$) owing to their centrosymmetric structure,[11] significant efforts have been made to overcome this constraint. Second-harmonic (SH) generation and phase modulation were demonstrated in Si waveguides with Si_3N_4 cladding.[12−14] In the early work by Jacobsen et al.,[12] it was shown that deposition of Si_3N_4 on a Si waveguide core would enable a linear EO effect and SH generation in the waveguide. An effective $\chi^{(2)}$ was presumed to be induced by stress at the core-cladding interface, yet, later, it was shown that the additional stress on the structure had no effect on the SH generation and that an ultraviolet exposure inhibited any frequency doubling.[15] Based on these results, the origin of $\chi^{(2)}$ in the waveguide was explained to be due to an electric field caused by trapped charge carriers on the material interfaces. The latter, coupled with third-order susceptibility ($\chi^{(3)}$), would lead to an effective second-order nonlinearity. The main drawback of the proposed approach based on symmetry breaking at the waveguide interface is that the

Received: June 10, 2022
Published: October 10, 2022

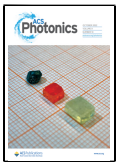

https://doi.org/10.1021/acsphotonics.2c00888
ACS Photonics 2022, 9, 3374−3383

overlap of the optical mode and nonlinear regions in the waveguide remains low, limiting the overall efficiency.[16] A way to circumvent this issue is through direct application of the external electric field across the waveguide core, as has been implemented via p−i−n junctions in Si waveguides.[17−19] In the proposed designs, applying a constant reverse bias voltage leads to a high DC electric field within the material, which allows phase modulation and SH generation efficiency control.

Alternatively, a permanent relocation of charge carriers inside the optical waveguide removes the requirement for the constant application of an external bias. For this purpose, all-optical poling (AOP) and electric-field poling can be used. Both of these techniques were initially employed in silica fibers.[20−24] In the AOP technique, the coherent photogalvanic effect is responsible for the asymmetric ionization of free charge carriers and the formation of space-charge grating due to interference of the fundamental light field and its SH.[25,26] On the other hand, the thermally assisted electric-field poling technique in silica fibers leveraged the fact that the charge carriers can be thermally activated and move in the presence of an externally applied electric field.[27−29] Such charge redistribution gives rise to an electric field inscription within the waveguide after electric-field poling. The induced $\chi^{(2)}$ in silica fibers using this technique was in the order of ∼0.1 pm/V estimated from phase modulation and SH generation experiments.[30,31] Recently, the possibility of AOP in Si_3N_4 integrated waveguides proved the availability of movable charge carriers within the material, enabling several applications such as efficient SH generation in microresonators,[32,33] generation of quantum states of light,[34] and simultaneous supercontinuum and SH generation.[35] Notably, the AOP process-determining parameters, such as concentration and diffusion coefficient of charge carriers responsible for the formation of the space-charge electric field and DC $\chi^{(3)}$ in Si_3N_4, have remained elusive. These are of key importance for fully establishing the potential of $\chi^{(2)}$ in nonlinear Si_3N_4 devices.

Here, we measure, for the first time to our knowledge, the DC $\chi^{(3)}$ in Si_3N_4 and demonstrate the formation of the permanent electric field residing exclusively within the Si_3N_4 waveguide core after thermally assisted electric-field poling. The latter is confirmed by two-photon microscopy (TPM) imaging. Hence, we obviate the requirement of applying a constant external DC field in order to access the linear EO effect on the platform. We also model the time evolution of charge carriers inside the Si_3N_4 waveguide under an applied electric field and calculate the inscribed field profile after the poling procedure. The implemented model is used to fit the poling dynamics and to extract the diffusion coefficient and number concentration of charge carriers involved in the process. The numerical optimization of the phase modulator suggests that for the same poling voltage, it is preferable to use wider waveguides in order to provide a larger overlap of an optical mode and an inscribed field in the $\chi^{(3)}$ medium.

EXPERIMENTAL DETAILS AND RESULTS

Refractive Index Modulation. In centrosymmetric materials, modulation of the refractive index can be introduced via the DC Kerr effect available through third-order nonlinearity $\chi^{(3)}$ and described by[11]

$$P_{\omega}^{(3)} = 3\epsilon_0\chi^{(3)}E_0^2E_{\omega}\, e^{j\omega t} + \text{c. c.} \quad (1)$$

where c.c. stands for the complex conjugate, $P_{\omega}^{(3)}$ is the third-order polarization at light frequency ω, ϵ_0 is the permittivity of free space, E_0 is the net electric field present in the material, and E_{ω} is the optical field propagating in the material. It is important to note that third-order susceptibility is a fourth-rank tensor; therefore, $\chi^{(3)}$, as used in eq 1, is E_0 and E_{ω} field direction-dependent. Here, we will consider two cases of relative polarization of the optical and electric fields inside a centrosymmetric material such as Si_3N_4. In such a case, two tensor elements are relevant: $\chi_{1111}^{(3)}$ and $\chi_{1122}^{(3)}$. For the optical field polarized parallel to the electrical field, the third-order susceptibility can be expressed as $\chi_{\text{eff}}^{(3)} = \chi_{1111}^{(3)}$, while for the case when fields have orthogonal relative polarization, $\chi_{\text{eff}}^{(3)} = \chi_{1122}^{(3)}$. We note that according to Kleinman's symmetry rule, it should follow that $\chi_{1111}^{(3)} = 3\chi_{1122}^{(3)}$.[11] Accordingly, for a material with a given refractive index n_0, the electric-field-induced refractive index change due to the DC Kerr effect is defined by[11]

$$\Delta n = \frac{3\chi_{\text{eff}}^{(3)}E_0^2}{2n_0} \quad (2)$$

The net electric field E_0 present in the waveguide can contain an inscribed field E_{ins}, an externally applied DC component E_{DC}, and a sinusoidal component with amplitude E_{m} at the modulation frequency ω_{m} such that

$$E_0 = E_{\text{ins}} + E_{\text{DC}} + E_{\text{m}}\ \sin(\omega_{\text{m}}t) \quad (3)$$

Here, we define $E_{\text{app}} = E_{\text{DC}} + E_{\text{m}}\sin(\omega_{\text{m}}t)$ to be the externally applied field. The expansion of the E_0^2 term in eq 2 reveals that the refractive index change has components at DC, ω_{m}, and $2\omega_{\text{m}}$ frequencies. The amplitude of the refractive index shift at each frequency is shown in Table 1. Henceforth, refractive index modulation at ω_{m} and $2\omega_{\text{m}}$ frequencies will be referred to as linear and quadratic EO effects, respectively, and indicate the relationship between the induced refractive index change with the modulation field E_{m} amplitude. Measurements of refractive index amplitude at modulation frequency ω_{m} and doubled modulation frequency $2\omega_{\text{m}}$ will be used for the extraction of effective third-order susceptibility $\chi_{\text{eff}}^{(3)}$. Similarly, we use the linear EO response in the Si_3N_4 before and after thermally assisted electric-field poling to account for electric field distribution and formation within the material. In this case, a static electric field present in the waveguide with $\chi_{\text{eff}}^{(3)}$ induces an effective second-order susceptibility $\chi_{\text{eff}}^{(2)}$ according to

$$\chi_{\text{eff}}^{(2)} = 3\chi_{\text{eff}}^{(3)}(E_{\text{DC}} + E_{\text{ins}}) \quad (4)$$

Table 1. Induced Refractive Index Change Recovered at DC, ω_{m} and $2\omega_{\text{m}}$ Frequencies

frequency	refractive index change Δn
DC	$\frac{3\chi_{\text{eff}}^{(3)}}{2n_0}\left[(E_{\text{DC}} + E_{\text{ins}})^2 + \frac{1}{2}E_{\text{m}}^2\right]$
ω_{m}	$\frac{3\chi_{\text{eff}}^{(3)}}{n_0}(E_{\text{DC}} + E_{\text{ins}})E_{\text{m}}$
$2\omega_{\text{m}}$	$\frac{3\chi_{\text{eff}}^{(3)}}{4n_0}E_{\text{m}}^2$

https://doi.org/10.1021/acsphotonics.2c00888
ACS Photonics 2022, 9, 3374−3383

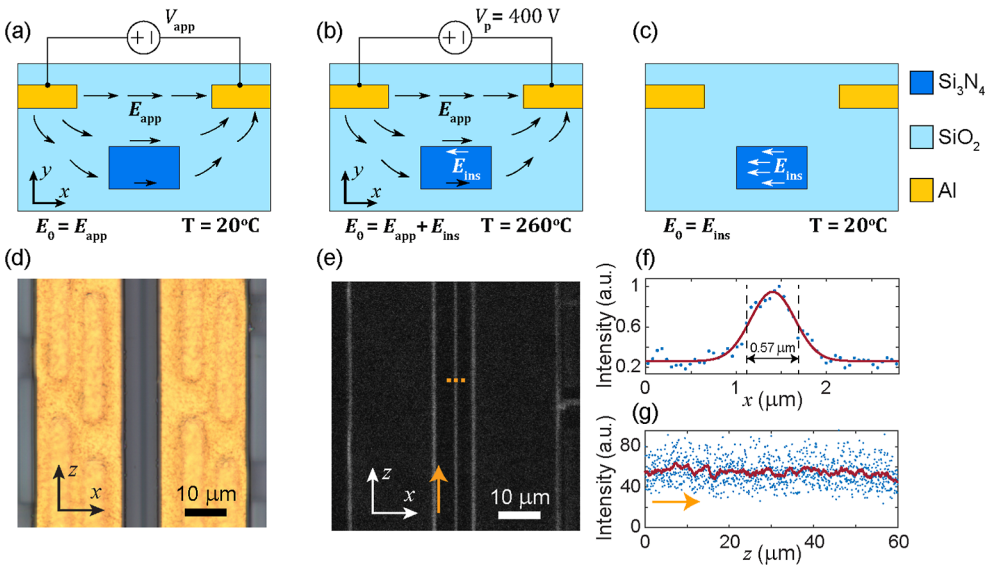

Figure 1. Schematic illustration of the device cross-section and electric field distribution (a) before, (b) during, and (c) after electric-field poling. V_{app} and V_p are the externally applied voltage and poling voltage, respectively. The device comprises a Si_3N_4 waveguide core buried in SiO_2 with aluminum electrodes (Al) along the waveguide. (d) Optical and (e) TPM images of the sample displaying received intensity of the SH signal P_{SH}. The images are recorded on the device comprising a Si_3N_4 waveguide with dimensions of 0.57 × 0.81 μm^2. (f) Profile of P_{SH} (blue dots) with fitting (FWHM = 0.57 μm) along the dashed orange line across the waveguide shown in (e). (g) Profile of P_{SH} (blue dots) detected along the waveguide as marked with the orange arrow in (e). In (g), the red solid line represents the moving average of P_{SH}.

It is important to note that throughout the study, the dispersion of $\chi^{(3)}_{eff}$ with respect to modulation frequency ω_m is assumed to be negligible such that $\chi^{(3)}_{eff}(\omega_m) \approx \chi^{(3)}_{eff}(0)$.

Device Design. The proposed Si_3N_4-based EO modulator is shown in Figure 1a–c, illustrating the principal cross-section and field distribution before, during, and after electric-field poling, respectively. In our study, two devices with different Si_3N_4 core dimensions of 1.31 × 0.81 μm^2 (wide) and 0.57 × 0.81 μm^2 (narrow) are used (see Supporting Information, Note 1). The electrodes are placed along the optical waveguide for an interaction length L and allow an application of the electric field in the sample plane. The total applied voltage (V_{app}) on the electrodes may have both DC (V_{DC}) and time-varying components (V_m) such that $V_{app} = V_{DC} + V_m$. In an unpoled waveguide, as in Figure 1a, the electric field applied across the waveguide will result in material refractive index change Δn due to the quadratic EO effect. The spatial distribution of the electric field and material properties define Δn in every point of the waveguide cross-section. Without any inscribed field present in the waveguide, the refractive index modulation at frequency ω_m is possible only if the externally applied field comprises a DC component, as evident from Table 1.

Figure 1b displays thermally assisted electric-field poling for electrical field inscription in Si_3N_4 waveguides. At the initial state, the charge carriers are immobile and uniformly distributed inside the waveguide core. The chip is heated up to enable thermal activation of charge carriers in Si_3N_4, while a high electric field is applied across the waveguide. The thermally activated mobile charges can migrate from their initial positions to compensate the externally applied field, forming a depleted region and, consequently, an inscribed electric field E_{ins} opposite to that applied. After a poling time of tens of minutes, the applied field is switched off, and the sample is translated to the metal surface for rapid cooling. The dislocated charges are fixed at new positions due to their low mobility at room temperature, establishing the steady space-charge electric field, as shown in Figure 1c. The inscribed electric field coupled with the third-order susceptibility of Si_3N_4 results in an effective second-order nonlinearity according to eq 4 and removes the requirement of an externally applied DC electric field for an observation of the linear EO effect.

The formation of the second-order nonlinearity solely within the Si_3N_4 waveguide core and not in the surrounding silica cladding is confirmed by TPM imaging (see Supporting Information, Note 2). During TPM imaging, a strong pump is raster-scanned across the waveguide plane, while the SH signal is collected. The received intensity of the SH signal P_{SH} at each point of the image is proportional to the square of the induced $\chi^{(2)}_{eff}$ and can be attributed to the recorded field within the waveguide such that $P_{SH} \sim (\chi^{(2)}_{eff})^2 \sim (\chi^{(3)} E_{ins})^2$. Figure 1d,e shows an optical photograph and a typical TPM image of the investigated area, respectively, obtained after electric-field poling. The lines on the sides of the TPM image indicate the nonlinear optical response on the electrode boundaries. The latter is present also in devices that have not undergone the thermally assisted electric-field poling and could be due to symmetry breaking at the metal–dielectric interface.[36] At the same time, there is an SH signal corresponding to the inscribed field confined to a narrow line along the waveguide between the electrodes in the center of the image. Notably, no SH active region is found inside the cladding. The full width at half maximum (FWHM) of SH response from the inscribed field is 0.57 ± 0.04 μm, coinciding with the waveguide width (Figure 1f). The TPM signal is consistent along the waveguide, as shown in Figure 1g, confirming a uniform inscription of a permanent electric field inside the Si_3N_4 waveguide core. Remarkably, we also observe the inscription of an electric field inside the waveguide in regions where only a single electrode is in the vicinity of the waveguide (see Supporting Information, Note 2). This finding suggests that electric-field poling with a

https://doi.org/10.1021/acsphotonics.2c00888
ACS Photonics 2022, 9, 3374–3383

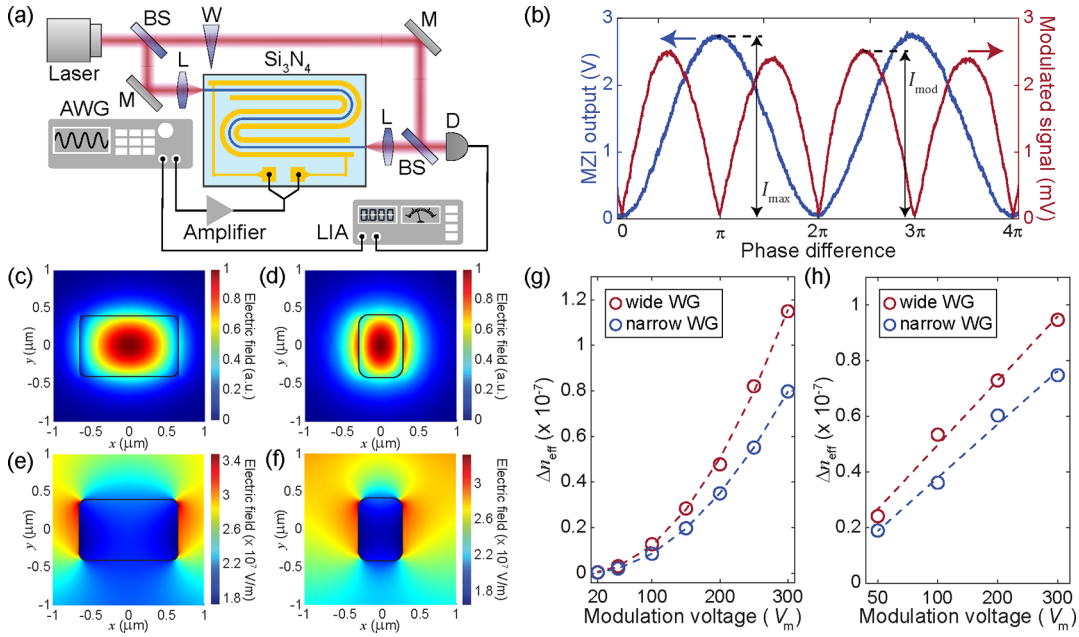

Figure 2. (a) Schematic of the MZI setup used for the phase modulation amplitude detection. BS: beam splitter, L: lens, AWG: arbitrary waveform generator, W: optical wedge, M: mirror, D: detector, and LIA: lock-in amplifier. (b) MZI output intensity (blue line) and modulation signal (red line) measured at $2\omega_m$ under applied modulation voltage on the electrodes of V_m = 100 V as a function of the relative phase difference between light in both arms in the waveguide with 1.31 × 0.81 μm^2 cross-section. (c,d) TE mode and (e,f) externally applied electric field (V_{DC} = 400 V) distribution in waveguides with 1.31 × 0.81 and 0.57 × 0.81 μm^2 cross-sections. (g) Effective refractive index change Δn_{eff} due to quadratic and (h) linear EO effect (under V_{DC} = 100 V) as a function of the modulation voltage V_m.

single electrode is possible. The latter has been leveraged for elevating maximal induced nonlinearity in electrically poled silica fibers.[37,38]

Experimental Setup. To measure the phase modulation due to linear and quadratic EO effects in Si_3N_4 waveguides, we used a Mach−Zehnder interferometric (MZI) technique,[39] as shown schematically in Figure 2a. In the setup, a linearly polarized laser operating at wavelength λ = 1560 nm is split into reference and sample arms. An optical wedge prism on a translation stage is placed in the path of the reference arm, enabling control of the relative phase difference between the light in both arms. The light in the sample arm is coupled to the Si_3N_4 waveguide placed onto a temperature controller stage in order to minimize the optical phase drift due to temperature variations. The output of the waveguide is combined with the light from the reference arm and directed to a photodetector. A signal from a function generator (Rohde & Schwarz HMF2525) is amplified by a voltage amplifier (Trek PZD350-2) and applied to the electrodes integrated alongside the waveguide, which will cause a phase change in the sample beam, leading to intensity modulation at the output of the MZI. A lock-in amplifier (Princeton Applied Research 5210) was used for the detection of the modulation amplitude to separate measurement of the linear and quadratic responses by recovering the modulated signal at ω_m and $2\omega_m$, respectively. During the measurements, the electric field modulation frequency was kept constant at ω_m = 5 kHz.

Figure 2b shows the measured MZI output intensity and the amplitude of the modulated signal at $2\omega_m$ as a function of the relative phase difference between light in both arms. Here, only modulation voltage with V_m = 100 V was applied between the electrodes. From the MZI output signal peak-to-peak value I_{max} and the amplitude of the modulated signal I_{mod}, we extract the phase variation $\Delta\phi$ at the quadrature point using[39]

$$\Delta\phi = 2\sin^{-1}\left(\frac{I_{mod}}{I_{max}}\right) \tag{5}$$

For a device having light and electric field interaction length L, the induced effective refractive index change is then calculated as $\Delta n_{eff} = \Delta\phi\lambda/2\pi L$. The effective refractive index change is determined by the degree of overlap between the optical and the electric fields in the waveguide core and in the cladding (see Supporting Information, Note 3). Taking into account both contributions, the effective refractive index change can be calculated using[40]

$$\Delta n_{eff} = 2c\epsilon_0 \iint n(x,y)\Delta n(x,y)|\boldsymbol{E}(x,y)|^2 \, dx \, dy \tag{6}$$

where $\Delta n(x,y)$ is the refractive index change according to Table 1, c is the speed of light in vacuum, and $\boldsymbol{E}(x,y)$ is the electric field profile of the optical mode propagating in the z direction normalized such that $\iint (E(x,y)^* \times \boldsymbol{E}(x,y) + \boldsymbol{E}(x,y) \times \boldsymbol{H}(x,y)^*)\hat{z} \, dx \, dy = 1$, where $\boldsymbol{H}(x,y)$ is the magnetic field profile of an optical mode. For known distributions of the parameters presented in eq 6, the contribution of the cladding and waveguide core can be calculated separately. A notable contribution to the total refractive index change in the narrow waveguide (≈21% and ≈15% in TE and TM polarization, respectively) is introduced by the quadratic EO effect in the waveguide cladding, despite the fact that third-order susceptibility of SiO_2 is expected to be one order of magnitude smaller than that of Si_3N_4. This is due to the penetration of the optical mode into the cladding, in which the applied electric field is actually higher than in the waveguide core. The latter is imposed by field continuity and the lower dielectric constant of SiO_2 compared to Si_3N_4. The fundamental optical mode profiles and the distributions of the applied electrical fields were simulated using COMSOL

https://doi.org/10.1021/acsphotonics.2c00888
ACS Photonics 2022, 9, 3374−3383

Multiphysics software and are as displayed in Figure 2c–f. The stronger confinement of an optical field inside the wide waveguide will result in a higher modulation of the refractive index than in the narrow waveguide since in the former, more of the optical field lies in the waveguide core, which has higher third-order nonlinearity. It should be noted that in the device, the applied electric field lies predominantly along the x-axis (see Supporting Information, Note 3). As mentioned above, this allows us to consider only the contribution of $\chi^{(3)}_{1111}$ or $\chi^{(3)}_{1122}$ tensor elements in a refractive index modulation when TE or TM polarized light, respectively, is coupled to the waveguide.

DC Kerr Susceptibility Measurements. Prior to electric-field poling, the quadratic and linear (with externally applied DC field) refractive index modulation was measured in the studied waveguides. Figure 2g shows the effective refractive index change dependence on modulation voltage V_m due to the quadratic EO effect in both wide and narrow waveguides using TE polarized light. As expected, effective refractive index change Δn_{eff} grows quadratically with the applied modulation voltage and is greater in the wide waveguide. To enable the linear EO effect in the device, a DC voltage V_{DC} = 100 V was applied in addition to a time-varying component, and effective refractive index modulation was recovered at ω_m (Figure 2h). Similarly, as in the case of the quadratic EO effect, the Δn_{eff} is larger in the wide waveguide. The ratio of the induced Δn_{eff} in the linear and quadratic regimes measured at the same voltage amplitudes ($V_{DC} = V_m$ = 100 V) is close to 4, as predicted (see Table 1).

For TM polarization of light, the same relationships of linear and quadratic regimes were observed (see Supporting Information, Note 4). Obtained results of the induced Δn_{eff} were then used for the derivation of the Si_3N_4 third-order susceptibility from eq 6, taking into account the silica cladding contribution. Following the formalism described in the Supporting Information, we calculate the average values of $\chi^{(3)}_{1111}$ and $\chi^{(3)}_{1122}$ of Si_3N_4 based on measurements carried out in both waveguides and both polarizations. The values are summarized in Table 2. To the best of our knowledge, this

Table 2. Derived Values of Si_3N_4 $\chi^{(3)}$ Tensor Elements in the Studied Waveguides

	1.31 × 0.81 μm^2	0.57 × 0.81 μm^2
$\chi^{(3)}_{1111}$ (× 10^{-21} m^2/V^2)	1.36 ± 0.08	1.40 ± 0.06
$\chi^{(3)}_{1122}$ (× 10^{-21} m^2/V^2)	0.75 ± 0.08	0.89 ± 0.08

is the first measurement of the DC Kerr susceptibility of Si_3N_4. Notably, the obtained $\chi^{(3)}_{1111}$ value is one order of magnitude higher than that of silica[41] and lower than the third-order susceptibility of Si_3N_4 measured at an optical frequency ($\chi^{(3)}(\lambda$ = 1.55 μm) = 3.4 × 10^{-21} m^2/V^2).[42,43] From Table 2, it is also evident that the ratio of $\chi^{(3)}_{1111}$ and $\chi^{(3)}_{1122}$, measured using TE and TM polarized light, respectively, is close to 2:1, which does not comply with Kleinman's symmetry rule. It should be noted that the assumption of the 3:1 ratio of $\chi^{(3)}_{1111}$ and $\chi^{(3)}_{1122}$ in silica is expected to have little influence on the extracted $\chi^{(3)}$ tensor element ratio in silicon nitride. For example, we calculate the contribution to the refractive index change from the cladding to be ≈3% and ≈2% for TE and TM polarized light, respectively, in the wide waveguide. Such small contributions cannot explain the deviation of the silicon nitride $\chi^{(3)}_{1111}/\chi^{(3)}_{1122}$ tensor element ratio from that suggested by Kleinman's symmetry rule. The reasons for this discrepancy are still unclear; however, similar violation was found earlier in other doped silica studies.[44]

Poling Dynamics. We performed a series of electric breakdown tests in devices of the same design and observed electrical breakdown on a chip surface at 650 V at room temperature. From this, the estimated breakdown field is 50 V/μm which is close to an order of magnitude less than reported elsewhere for SiO_2 and Si_3N_4.[45,46] The reason for this lies in the fabrication process, particularly in the step of metal layer etching, small metal residues are expected to be present, which may have introduced local breakdown channels when the high electric field is applied. Hence, the poling voltage V_p was set at 400 V in order to avoid electric breakdown. Both waveguides were then poled at 260 °C in a series of treatments, and after each, linear and quadratic responses were measured at different modulation voltages. After each poling interval, the linear EO effect was observed in the devices without any externally applied DC voltage, confirming the formation of a space-charge field inside the waveguides. Figure 3a shows the effective refractive index change Δn_{eff} per V_m for TE polarized

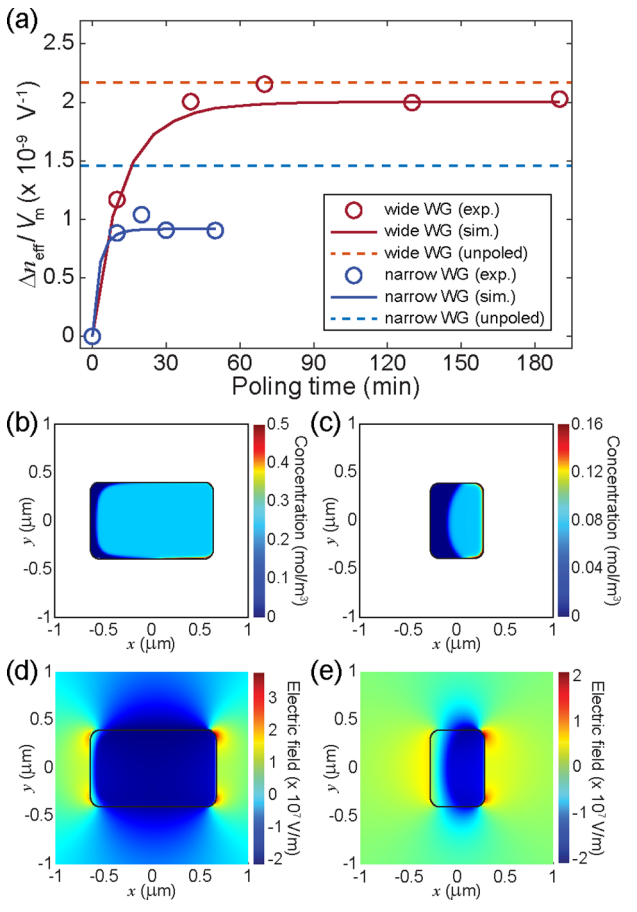

Figure 3. (a) Effective refractive index change Δn_{eff} per V_m (points) measured in both waveguides at ω_m after each electric-field poling interval using TE polarized light. Poling was performed at 260 °C and 400 V applied between the electrodes. The solid lines are the fits based on charge species drift simulation, while dashed lines correspond to Δn_{eff} per V_m measured before poling at frequency ω_m with 400 V DC field applied ($V_{DC} = V_p$ = 400 V). (b,c) Simulated positive charge carrier distribution in the wide and narrow Si_3N_4 waveguides, respectively, after electric-field poling. (d,e) inscribed electric field distribution E_{ins} after electric-field poling.

https://doi.org/10.1021/acsphotonics.2c00888
ACS Photonics 2022, 9, 3374–3383

light measured in both devices at ω_m after each poling interval. As evident, Δn_{eff} saturates after several tens of minutes of poling.

The saturation dynamics of Δn_{eff} in Figure 3a tend to suggest that the electric-field poling process is governed by one species. This is in contrast to electric-field poling of silica fibers, where the injection of H_3O^+ produced by high field ionization on the anode surface has been observed in the case of a long poling time.[27] The latter was also shown to result in a drop of the induced nonlinearity due to neutralization of the uncompensated negative charges. In addition, Figure 3a also holds the Δn_{eff} per V_m as measured in unpoled waveguides at ω_m with DC voltage $V_{DC} = V_p = 400$ V applied. Notably, the saturation value of Δn_{eff} per V_m after poling at $V_p = 400$ V is less than that measured before poling with $V_{DC} = 400$ V applied on the electrodes. Moreover, the mismatch is larger in the narrower waveguide in which the device efficiency is just ≈60% of that achieved with the externally applied DC field.

To explain this observation, a two-dimensional model based on the solution of transport of diluted species was developed. The latter is used for simulation of the dynamics and saturation of the electric-field poling process. Our model, made in COMSOL Multiphysics, follows that described in the study by Camara et al.[47] and allows us to simulate the charge carrier drift under an applied electric field. It is expected that the experimentally obtained electric-field poling curves are directly related to the charge carrier properties, such as their diffusion coefficient and number concentration. In the simulation, we initially set the waveguide to be electrically neutral, having positively and negatively charged species to be evenly distributed inside the waveguide core. We then bound the charge carrier drift to take place only inside the waveguide core, as well as set only one charge carrier specimen to be mobile. The actual sign of the mobile charge carrier is unknown, and for the simulation, it was chosen to be positive. In the assumption of no charge carrier injection, the local equation of continuity and Poisson's equation lead to the following partial differential equation solved over waveguide cross-section and time[47]

$$\frac{\partial C}{\partial t} + \nabla\cdot(-D\nabla C - q\mu FC\nabla u) = 0 \tag{7}$$

where C is the concentration of initially uniformly distributed diluted cations, D is the diffusion coefficient, q is the charge (here +1 for cations), μ is the charge mobility, F is Faraday's constant, and u is the electric potential. In eq 7, the first term inside the brackets accounts for the charge diffusion, while the second term corresponds to the charge drift under the electric field. D is coupled to the mobility μ through the relation $\mu = qFD/RT$, where R is the molar gas constant and T is the sample temperature. Using the implemented model, the charge concentration and the diffusion coefficient were varied to fit the dynamics of the electric-field poling process in the studied waveguides. Notably, we find that the number concentration of mobile charges will determine the saturation value Δn_{eff}, while both charge concentration and diffusion coefficient contribute to the poling speed. The fits of the electric-field poling curves are shown by solid lines in Figure 3a. From these, we obtain the number concentration of charges to be $C = 0.24 \pm 0.13$ mol/m^3 ($C = 0.075 \pm 0.01$ mol/m^3) and the diffusion coefficient at 260 °C to be $D = (0.45 \pm 0.18) \times 10^{-18}$ m^2/s ($D = (3.6 \pm 1.8) \times 10^{-18}$ m^2/s) in the wide (narrow) waveguide. It should be noted that only the low bound of the diffusion coefficient value can be estimated from the poling dynamics fit of the narrow waveguide due to the absence of an intermediate point between poling start and saturation of the refractive index change in the linear regime. A slight discrepancy in the charge number concentration values obtained from the narrow and wide waveguide poling curve fits is predominantly introduced by the measurement error of induced effective nonlinearity and a small number of fitting points (see Supporting Information, Note 5).

From the extracted charge carrier parameters, we cannot unambiguously confirm the species of mobile ions inside Si_3N_4. However, earlier reports have shown that there is an excessive amount of hydrogen present in low pressure chemical vapor-deposited Si_3N_4.[48] Moreover, the measured range of hydrogen diffusion coefficient D in Si_3N_4 summarized in ref 49 matches well the value obtained in this study. Hence, we tend to believe that hydrogen impurities could be responsible for space-charge field formation in the waveguides studied here.

Figure 3b,c shows the simulated profiles of the mobile charge carrier distribution in both waveguides after poling with $V_p = 400$ V applied between the electrodes. The simulation shows that, in order to compensate the electric field in the waveguide applied during poling, the charge carriers have drifted, causing the appearance of a depletion region—a region in the waveguide core where there is a reduced number of cations. As evident from Figure 3b,c, the depletion region can take a significant part of the waveguide core. From the simulation, we also can extract the final inscribed electric field E_{ins} in both waveguides, as shown in Figure 3d,e. From the latter, it can be concluded that the inscribed field E_{ins} in the depletion region is weaker than in the rest of the waveguide core. Hence, the contribution of the depletion region to the inscribed nonlinearity experienced by the optical mode is small. The maximal inscribed electric field is ≈20 V/μm for the wide waveguide, resulting in the effective induced second-order susceptibility (eq 4) of 0.084 pm/V. The mismatch between the Δn_{eff} saturation value after poling and that expected from linear EO effect measurements with externally applied DC field, as shown in Figure 3a, is simply due to the fact that the distribution of the inscribed field E_{ins} does not match that of the externally applied one. The mismatch of the induced nonlinearity is relatively low in the wide waveguide since the depletion region takes the part of the core far from the maximal optical field, while in the narrow waveguide, the interaction of the propagating optical mode and the inscribed electric field is less efficient, explaining the larger difference of the induced nonlinearity with the case of the externally applied field. In addition to this, the inscribed field E_{ins} after poling resides exclusively inside the waveguide core as confirmed by TPM, and, therefore, there is no contribution to the linear EO effect by the silica cladding.

It is worth noting that if the number concentration of charge carriers C and the applied electric field during poling are known, the width of the depletion region w can be approximately estimated using[50]

$$w = \frac{\epsilon\epsilon_0 E_{DC}}{eC} \tag{8}$$

where E_{DC} is the externally applied DC field during poling, ϵ is the dielectric permittivity of a material, and e is the elementary charge. For example, assuming $C = 0.24$ mol/m^3 retrieved from the poling dynamics fit, as shown above for the wide waveguide, we calculate the thickness of the depletion layer

https://doi.org/10.1021/acsphotonics.2c00888
ACS Photonics 2022, 9, 3374−3383

for the poling voltage of 400 V to be around 0.06 μm, which, in principle, is in good agreement with the value obtained from numerical simulation (see Figure 3b). Such an approximate estimation of the depletion region width using eq 8, instead of charge carrier drift numerical simulation, can be used for a coarse evaluation of effective induced nonlinearity experienced by the optical mode.

After electric-field poling, the E_{ins} inside the waveguides decays slowly. In Figure 4a, we show the induced Δn_{eff} per V_m

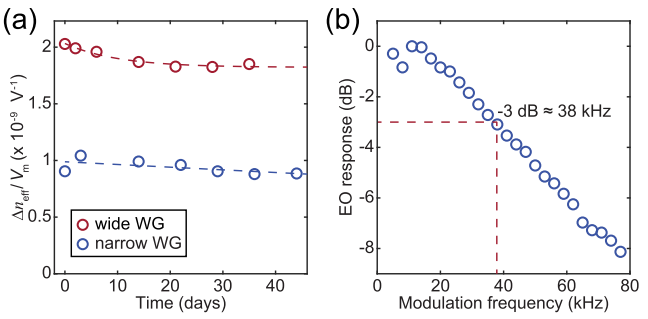

Figure 4. (a) Decay of effective refractive index change Δn_{eff} per V_m (points) measured in both waveguides after electric-field poling. Dashed lines are guides for the eye. (b) EO response of a device (points) comprising poled Si_3N_4 waveguide with 0.57 μm width and the active modulation length of L = 83 mm.

measured over a period of 1 month. Within the measurement period, the amplitude of the induced second-order nonlinearity decreased by ≈10% of its initial values. The decay time is similar to that obtained for all-optically induced nonlinear gratings,[51] suggesting that the same charge carriers are activated in both poling processes. We also measured the EO response of a device comprising poled Si_3N_4, as shown in Figure 4b. The obtained 3 dB modulation bandwidth for the waveguide with 0.57 μm width was measured to be 38 kHz (Figure 4b). We believe that the bandwidth limitation is due to the time constant of the measurement system, having a strong contribution from the high output load of the test equipment, the ohmic contact between electrodes and probes, and the high capacitance of the latter. At the same time, it is important to note that the proposed device design itself should have a low capacitance due to the small overlapping area and the large separation between the electrodes.

Based on the experimentally derived nonlinear parameters and the developed model for charge carrier drift in the waveguide core, we simulate the electric-field poling process in waveguides with different widths for various applied poling voltages, as to estimate maximal achievable nonlinearity in a device with the same configuration as studied here. In the sweep, the poling voltage was varied from 400 to 3400 V, while the waveguide width was changed from 0.5 to 2.5 μm. The charge carrier concentration is set to be C = 0.24 mol/m^3, as extracted from poling dynamics fit for the case of the wide waveguide. It should be pointed out that here, we used the highest calculated charge carrier concentration, which would lead to the smallest depletion region width and, hence, the highest induced effective refractive change after electric-field poling. Also, the upper voltage limit was chosen such that the induced electric field is below the reported breakdown field of 300 V/μm in Si_3N_4.[46] It is important to note that the current fabrication process has been considerably improved with respect to the one used for the devices described here, allowing us to avoid metal residues and related breakdown field limitations. Hence, we believe that the application of 300 V/μm during the electric-field poling process should be possible in devices of the same design, as proposed in this work. In the numerical simulation, for each combination of applied voltage and set waveguide width in the simulation, the saturation of the poling process was reached. At the end of the simulation, the inscribed electric field E_{ins} was extracted and the induced Δn_{eff} per V_m was calculated numerically using eq 6. The height of the waveguide was kept constant at 0.81 μm. The obtained values are mapped in Figure 5a.

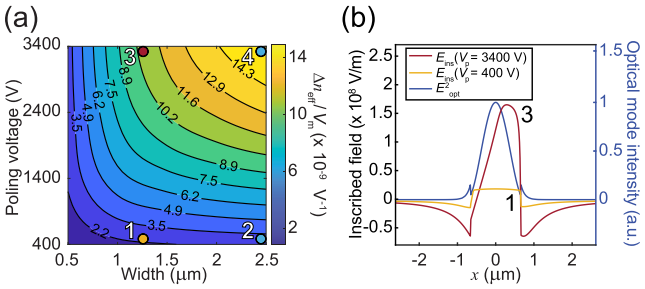

Figure 5. (a) Normalized induced effective index change per V_m in an electrically poled Si_3N_4 waveguide as a function of waveguide width and poling voltage. (b) Inscribed electric field E_{ins} profiles across the optical waveguide with 1.31 μm width poled at 400 and 3400 V plotted on the primary axis. The normalized optical mode intensity profile across the same waveguide is plotted on the secondary axis. (1) and (3) correspond to points as labeled in (a).

Here, we have also highlighted four points marking the Δn_{eff} per V_m for particular waveguide width and poling voltage. The first point (1) corresponds to Δn_{eff} per V as achieved in the waveguide with 1.31 μm width used in this study poled at V_p = 400 V. The second point (2) indicates the Δn_{eff} per V_m for the case when poling at V_p = 400 V would be carried out on a waveguide with a width of 2.5 μm. We see that by increasing the waveguide width from 1.31 to 2.5 μm, the achievable effective refractive index change is increased just by ≈20%. The confinement of the optical mode in waveguides of mentioned widths and the narrow depletion region width at the given poling voltage result in the moderate growth of effective refractive index change. Significant improvement of the induced nonlinearity would be achieved in case poling voltage of V_p = 3400 V as marked by points (3) and (4). By elevating the poling voltage from 400 V to 3400 V, we expect a ≈5.4 times increase in the effective refractive index change in the waveguide having 1.31 μm width and ≈6.3 times increase in the waveguide having 2.5 μm width. The growth of the induced nonlinearity is not linearly dependent on poling voltage which can be illustrated and explained by considering the inscribed electric field E_{ins} and optical mode intensity profiles shown in Figure 5b. Here, the inscribed electric field E_{ins} in a 1.31 μm-wide Si_3N_4 waveguide is displayed for two cases when poling voltage is V_p = 400 V and V_p = 3400 V. The maximal values of the inscribed field for the poling voltages of 400 and 3400 V are ≈20 V/μm and ≈173 V/μm for the waveguide with 1.31 μm width, resulting in the effective induced second-order susceptibility (eq 4) of 0.084 and 0.73 pm/V, respectively, while considering the breakdown strength of Si_3N_4 of 300 V/μm, the maximal achievable effective second-order susceptibility is ≈1.26 pm/V. It is important to note that with an increase in poling voltage, the depletion

https://doi.org/10.1021/acsphotonics.2c00888
ACS Photonics 2022, 9, 3374−3383

region takes a larger part of the waveguide core, shifting the maximum value of the inscribed field toward the ground electrode and, therefore, changing the optical mode and inscribed field overlap condition. Additionally, from Figure 5a, it is important to notice that for every waveguide width, there is a poling voltage level, above which the induced effective refractive index change would not increase. For a specific waveguide width and charge concentration, the maximal inscribed electric field is defined using eq 8. It can be seen in Figure 5a that in the regions where contour lines become vertical, a further increase in the poling voltage (or the applied electric field) would not lead to a growth of the induced refractive index change for a given waveguide width.

CONCLUSIONS AND OUTLOOK

In this work, we have demonstrated a linear EO modulation in the Si_3N_4 platform. For the first time, we measured the $\chi^{(3)}$ of Si_3N_4 at low frequencies and induced symmetry breaking inside the Si_3N_4 waveguides through thermally assisted electric-field poling. During the poling process, the thermally activated charge carriers drift such that the externally applied electric field is compensated. After waveguide cooling, the trapped charge carriers form an inscribed electric field that induces an effective second-order nonlinearity. The latter removes the requirement of the externally applied DC electric field for making the linear EO effect accessible in a fully CMOS fabrication process-compatible integrated photonic platform. Notably, the charge carrier drift during poling takes place only inside the Si_3N_4 waveguide core, as confirmed by nonlinear imaging. From the numerical simulation of the process and experimental poling curve fit, we extract the diffusion coefficient and the concentration of charge carriers responsible for the electric-field inscription within Si_3N_4. Further studies on the initial stage of poling dynamics and an extension of the physical model, for example, including charge transfer at the waveguide core-cladding boundary, would be necessary in the future. Despite that, the extracted diffusion coefficient and charge carrier concentration values and those reported from earlier Si_3N_4 material analysis studies lead us to believe that hydrogen impurities could be responsible for space-charge field formation. Here, in the waveguide core, the inscribed electric field as high as 20 V/μm is achieved and limited only by the electrical breakdown of the cladding layer. Given that the dielectric strength of employed materials could be increased to the values reported in the literature, we estimated that the inscribed field in the waveguide could reach 300 V/μm, leading to a $\chi^{(2)}$ in Si_3N_4 of around ~1 pm/V. Furthermore, there could be several strategies for increasing the induced second-order nonlinearity in the device of the proposed design. First, following eq 8, it can be suggested that having more charge carriers, for example, by introducing dopants in the Si_3N_4 waveguide during the fabrication process, would allow us to increase the inscribed effective nonlinearity as more applied field could be compensated by the charge carriers. Second, eq 4 implies that using the waveguide core material with a higher $\chi^{(3)}$ value would allow us to increase the efficiency of the device of the same design. For the proposed linear EO phase modulation application, we suspect that silicon-rich silicon nitride[52] could be a good candidate. Other methods for charge activation can be implemented. For example, in silica fibers, it was demonstrated that light of high-energy photons can be used for the charge release and used for electric-field poling.[53,54] Based on the reported results, further material and device design improvements could enable fully CMOS fabrication process-compatible second-order nonlinear Si_3N_4 devices for classical and quantum applications.

ASSOCIATED CONTENT

Supporting Information

The Supporting Information is available free of charge at https://pubs.acs.org/doi/10.1021/acsphotonics.2c00888.

Sample description, two-photon microscopy imaging, refractive index change calculation, linear and quadratic electro-optic effects with TM polarized light, and poling dynamics simulations (PDF)

AUTHOR INFORMATION

Corresponding Author

Camille-Sophie Brès − *Photonic Systems Laboratory (PHOSL), Ecole Polytechnique Fédérale de Lausanne, STI-IEM, Lausanne CH-1015, Switzerland*; Email: camille.bres@epfl.ch

Authors

Boris Zabelich − *Photonic Systems Laboratory (PHOSL), Ecole Polytechnique Fédérale de Lausanne, STI-IEM, Lausanne CH-1015, Switzerland*; orcid.org/0000-0002-8542-7542

Edgars Nitiss − *Photonic Systems Laboratory (PHOSL), Ecole Polytechnique Fédérale de Lausanne, STI-IEM, Lausanne CH-1015, Switzerland*; orcid.org/0000-0001-9577-9958

Anton Stroganov − *LIGENTEC SA, Ecublens CH-1024, Switzerland*

Complete contact information is available at: https://pubs.acs.org/10.1021/acsphotonics.2c00888

Funding

The funding was provided by ERC grant PISSARRO (ERC-2017-CoG 771647).

Notes

The authors declare no competing financial interest.

REFERENCES

(1) Zhang, M.; Buscaino, B.; Wang, C.; Shams-Ansari, A.; Reimer, C.; Zhu, R.; Kahn, J. M.; Lončar, M. Broadband electro-optic frequency comb generation in a lithium niobate microring resonator. *Nature* **2019**, *568*, 373−377.

(2) Geler-Kremer, J.; Eltes, F.; Stark, P.; Stark, D.; Caimi, D.; Siegwart, H.; Jan Offrein, B.; Fompeyrine, J.; Abel, S. A ferroelectric multilevel non-volatile photonic phase shifter. *Nat. Photonics* **2022**, *16*, 491.

(3) Snigirev, V.; et al.Ultrafast tunable lasers using lithium niobate integrated photonics. December 3, 2021, arXiv (Physics, Optics), arXiv:2112.02036. https://arxiv.org/abs/2112.02036v3 (accessed Aug 11, 2022).

(4) Rahim, A.; Hermans, A.; Wohlfeil, B.; Petousi, D.; Kuyken, B.; Van Thourhout, D.; Baets, R. Taking silicon photonics modulators to a higher performance level: state-of-the-art and a review of new technologies. *Adv. Photonics* **2021**, *3*, 024003.

(5) Borghi, M.; Castellan, C.; Signorini, S.; Trenti, A.; Pavesi, L. Nonlinear silicon photonics. *J. Opt.* **2017**, *19*, 093002.

(6) Leuthold, J.; Koos, C.; Freude, W. Nonlinear Silicon Photonics. *Nat. Photonics* **2010**, *4*, 535−544.

(7) Moss, D.; Morandotti, R.; Gaeta, A.; Lipson, M. New CMOS-compatible platforms based on silicon nitride and Hydex for nonlinear optics. *Nat. Photonics* **2013**, *7*, 597−607.

(8) Gaeta, A. L.; Lipson, M.; Kippenberg, T. J. Photonic-chip-based frequency combs. *Nat. Photonics* **2019**, *13*, 158−169.
(9) Reed, G. T.; Jason Png, C. J. Silicon optical modulators. *Mater. Today* **2005**, *8*, 40−50.
(10) Silverstone, J. W.; Bonneau, D.; O'Brien, J. L.; Thompson, M. G. Silicon Quantum Photonics. *IEEE J. Sel. Top. Quantum Electron.* **2016**, *22*, 390−402.
(11) Boyd, R. W.*Nonlinear Optics*, 3rd ed.; Academic Press, Inc.: USA, 2008.
(12) Jacobsen, R. S.; Andersen, K. N.; Borel, P. I.; Fage-Pedersen, J.; Frandsen, L. H.; Hansen, O.; Kristensen, M.; Lavrinenko, A. V.; Moulin, G.; Ou, H.; Peucheret, C.; Zsigri, B.; Bjarklev, A. Strained silicon as a new electro-optic material. *Nature* **2006**, *441*, 199−202.
(13) Chmielak, B.; Waldow, M.; Matheisen, C.; Ripperda, C.; Bolten, J.; Wahlbrink, T.; Nagel, M.; Merget, F.; Kurz, H. Pockels effect based fully integrated, strained silicon electro-optic modulator. *Opt. Express* **2011**, *19*, 17212−17219.
(14) Cazzanelli, M.; Bianco, F.; Borga, E.; Pucker, G.; Ghulinyan, M.; Degoli, E.; Luppi, E.; Véniard, V.; Ossicini, S.; Modotto, D.; Wabnitz, S.; Pierobon, R.; Pavesi, L. Second-harmonic generation in silicon waveguides strained by silicon nitride. *Nat. Mater.* **2012**, *11*, 148−154.
(15) Castellan, C.; Trenti, A.; Vecchi, C.; Marchesini, A.; Mancinelli, M.; Ghulinyan, M.; Pucker, G.; Pavesi, L. On the origin of second harmonic generation in silicon waveguides with silicon nitride cladding. *Sci. Rep.* **2019**, *9*, 1088.
(16) Berciano, M.; Marcaud, G.; Damas, P.; Le Roux, X.; Crozat, P.; Alonso Ramos, C.; Pérez Galacho, D.; Benedikovic, D.; Marris-Morini, D.; Cassan, E.; et al. Fast linear electro-optic effect in a centrosymmetric semiconductor. *Commun. Phys.* **2018**, *1*, 64.
(17) Timurdogan, E.; Poulton, C. V.; Byrd, M. J.; Watts, M. R. Electric field-induced second-order nonlinear optical effects in silicon waveguides. *Nat. Photonics* **2017**, *11*, 200−206.
(18) Franchi, R.; Castellan, C.; Ghulinyan, M.; Pavesi, L. Second-harmonic generation in periodically poled silicon waveguides with lateral p-i-n junctions. *Opt. Lett.* **2020**, *45*, 3188−3191.
(19) Chakraborty, U.; Carolan, J.; Clark, G.; Bunandar, D.; Gilbert, G.; Notaros, J.; Watts, M. R.; Englund, D. R. Cryogenic operation of silicon photonic modulators based on the DC Kerr effect. *Optica* **2020**, *7*, 1385−1390.
(20) Österberg, U.; Margulis, W. Dye laser pumped by Nd:YAG laser pulses frequency doubled in a glass optical fiber. *Opt. Lett.* **1986**, *11*, 516−518.
(21) Kazansky, P. G.; Dong, L.; Russell, P. S. J. High second-order nonlinearities in poled silicate fibers. *Opt. Lett.* **1994**, *19*, 701−703.
(22) Stolen, R. H.; Tom, H. W. K. Self-organized phase-matched harmonic generation in optical fibers. *Opt. Lett.* **1987**, *12*, 585−587.
(23) Fujiwara, T.; Wong, D.; Fleming, S. Large electrooptic modulation in a thermally-poled germanosilicate fiber. *IEEE Photon. Technol. Lett.* **1995**, *7*, 1177−1179.
(24) Kazansky, P. G.; Pruneri, V. Electric-field poling of quasi-phase-matched optical fibers. *JOSA B* **1997**, *14*, 3170−3179.
(25) Anderson, D. Z.; Mizrahi, V.; Sipe, J. E. Model for second-harmonic generation in glass optical fibers based on asymmetric photoelectron emission from defect sites. *Opt. Lett.* **1991**, *16*, 796−798.
(26) Dianov, E. M.; Starodubov, D. S. Photoinduced generation of the second harmonic in centrosymmetric media. *Quantum Electron.* **1995**, *25*, 395−407.
(27) Alley, T. G.; Brueck, S.; Wiedenbeck, M. Secondary ion mass spectrometry study of space-charge formation in thermally poled fused silica. *J. Appl. Phys.* **1999**, *86*, 6634−6640.
(28) Faccio, D.; Pruneri, V.; Kazansky, P. G. Dynamics of the second-order nonlinearity in thermally poled silica glass. *Appl. Phys. Lett.* **2001**, *79*, 2687−2689.
(29) Kudlinski, A.; Quiquempois, Y.; Martinelli, G. Modeling of the $\chi(2)$ susceptibility time-evolution in thermally poled fused silica. *Opt. Express* **2005**, *13*, 8015−8024.
(30) Tarasenko, O.; Margulis, W. Electro-optical fiber modulation in a Sagnac interferometer. *Opt. Lett.* **2007**, *32*, 1356−1358.
(31) Pruneri, V.; Kazansky, P. G. Electric-field thermally poled optical fibers for quasi-phase-matched second-harmonic generation. *IEEE Photon. Technol. Lett.* **1997**, *9*, 185−187.
(32) Lu, X.; Moille, G.; Rao, A.; Westly, D. A.; Srinivasan, K. Efficient photoinduced second-harmonic generation in silicon nitride photonics. *Nat. Photonics* **2021**, *15*, 131−136.
(33) Nitiss, E.; Hu, J.; Stroganov, A.; Brès, C.-S. Optically reconfigurable quasi-phase-matching in silicon nitride microresonators. *Nat. Photonics* **2022**, *16*, 134−141.
(34) Dalidet, R.; Mazeas, F.; Nitiss, E.; Yakar, O.; Stroganov, A.; Tanzilli, S.; Labonté, L.; Brès, C.-S. Near perfect two-photon interference out of a down-converter on a silicon photonic chip. *Opt. Express* **2022**, *30*, 11298−11305.
(35) Hickstein, D. D.; Carlson, D. R.; Mundoor, H.; Khurgin, J. B.; Srinivasan, K.; Westly, D.; Kowligy, A.; Smalyukh, I. I.; Diddams, S. A.; Papp, S. B. Self-organized nonlinear gratings for ultrafast nanophotonics. *Nat. Photonics* **2019**, *13*, 494−499.
(36) Bachelier, G.; Butet, J.; Russier-Antoine, I.; Jonin, C.; Benichou, E.; Brevet, P.-F. Origin of optical second-harmonic generation in spherical gold nanoparticles: Local surface and nonlocal bulk contributions. *Phys. Rev. B* **2010**, *82*, 235403.
(37) Margulis, W.; Tarasenko, O.; Myrén, N. Who needs a cathode? Creating a second-order nonlinearity by charging glass fiber with two anodes. *Opt. Express* **2009**, *17*, 15534−15540.
(38) De Lucia, F.; Bannerman, R.; Englebert, N.; Nunez Velazquez, M. M. A. N.; Leo, F.; Gates, J.; Gorza, S.-P.; Sahu, J.; Sazio, P. J. A. Single is better than double: theoretical and experimental comparison between two thermal poling configurations of optical fibers. *Opt Express* **2019**, *27*, 27761−27776.
(39) Wong, D.; Xu, W.; Fleming, S.; Janos, M.; Lo, K. M. Frozen-in Electrical Field in Thermally Poled Fibers. *Opt. Fiber Technol.* **1999**, *5*, 235−241.
(40) Kogelnik, H.*Integrated Optics*; Springer, 1975; pp 13−81.
(41) Liu, A. C.; Digonnet, M. J. F.; Kino, G. S. Measurement of the dc Kerr and electrostrictive phase modulation in silica. *JOSA B* **2001**, *18*, 187−194.
(42) Ikeda, K.; Saperstein, R. E.; Alic, N.; Fainman, Y. Thermal and Kerr nonlinear properties of plasma-deposited silicon nitride/silicon dioxide waveguides. *Opt. Express* **2008**, *16*, 12987−12994.
(43) Gao, M.; Yang, Q.-F.; Ji, Q.-X.; Wang, H.; Wu, L.; Shen, B.; Liu, J.; Huang, G.; Chang, L.; Xie, W.; et al. Probing material absorption and optical nonlinearity of integrated photonic materials. *Nat. Commun.* **2022**, *13*, 3323.
(44) Liu, A. C.; Digonnet, M. J. F.; Kino, G. S.DC Kerr measurement in a silica channel waveguide. *Proceedings SPIE 2841, Doped Fiber Devices*, 1996; pp 209−218.
(45) Kazansky, P.; Pruneri, V. Electrically stimulated light-induced second-harmonic generation in glass: evidence of coherent photoconductivity. *Phys. Rev. Lett.* **1997**, *78*, 2956.
(46) Rauthan, C.; Srivastava, J. Electrical breakdown voltage characteristics of buried silicon nitride layers and their correlation to defects in the nitride layer. *Mater. Lett.* **1990**, *9*, 252−258.
(47) Camara, A.; Tarasenko, O.; Margulis, W. Study of thermally poled fibers with a two-dimensional model. *Opt. Express* **2014**, *22*, 17700−17715.
(48) Pfeiffer, M. H.; Liu, J.; Raja, A. S.; Morais, T.; Ghadiani, B.; Kippenberg, T. J. Ultra-smooth silicon nitride waveguides based on the Damascene reflow process: fabrication and loss origins. *Optica* **2018**, *5*, 884−892.
(49) Morin, P. F.; Pelletier, B.; Laffosse, E.; Plantier, L. Modeling stress development and hydrogen diffusion in plasma enhanced chemical vapor deposition silicon nitride films submitted to thermal cycles. *J. Appl. Phys.* **2013**, *114*, 154113.
(50) von Hippel, A.; Gross, E. P.; Jelatis, J. G.; Geller, M. Photocurrent, Space-Charge Buildup, and Field Emission in Alkali Halide Crystals. *Phys. Rev.* **1953**, *91*, 568−579.

https://doi.org/10.1021/acsphotonics.2c00888
ACS Photonics 2022, 9, 3374−3383

(51) Nitiss, E.; Liu, T.; Grassani, D.; Pfeiffer, M.; Kippenberg, T. J.; Brès, C.-S. Formation Rules and Dynamics of Photoinduced $\chi^{(2)}$ Gratings in Silicon Nitride Waveguides. *ACS Photonics* **2020**, *7*, 147−153.
(52) Lin, H.-H.; Sharma, R.; Friedman, A.; Cromey, B. M.; Vallini, F.; Puckett, M. W.; Kieu, K.; Fainman, Y. On the observation of dispersion in tunable second-order nonlinearities of silicon-rich nitride thin films. *APL Photonics* **2019**, *4*, 036101.
(53) Camara, A. R.; Pereira, J. M.; Tarasenko, O.; Margulis, W.; Carvalho, I. C. Optical creation and erasure of the linear electrooptical effect in silica fiber. *Opt. Express* **2015**, *23*, 18060−18069.
(54) Pereira, J. M.; Camara, A. R.; Laurell, F.; Tarasenko, O.; Margulis, W. Linear electro-optical effect in silica fibers poled with ultraviolet lamp. *Opt. Express* **2019**, *27*, 14893−14902.

https://doi.org/10.1021/acsphotonics.2c00888
ACS Photonics 2022, 9, 3374−3383